Diagenetic formation of uranium-silica polymers in lake sediments over 3,300 years

Pierre Lefebvre, Alkiviadis Gourgiotis, Arnaud Mangeret, Pierre Sabatier, Pierre Le Pape, Olivier Diez, Pascale Louvat, Nicolas Menguy, Pauline Merrot, Camille Baya, et al.

▶ **To cite this version:**

Pierre Lefebvre, Alkiviadis Gourgiotis, Arnaud Mangeret, Pierre Sabatier, Pierre Le Pape, et al.. Diagenetic formation of uranium-silica polymers in lake sediments over 3,300 years. Proceedings of the National Academy of Sciences of the United States of America, 2021, 118 (4), 10.1073/pnas.2021844118 . hal-03963873v2

HAL Id: hal-03963873
https://hal.science/hal-03963873v2

Submitted on 15 Mar 2023

HAL is a multi-disciplinary open access archive for the deposit and dissemination of scientific research documents, whether they are published or not. The documents may come from teaching and research institutions in France or abroad, or from public or private research centers.

L'archive ouverte pluridisciplinaire **HAL**, est destinée au dépôt et à la diffusion de documents scientifiques de niveau recherche, publiés ou non, émanant des établissements d'enseignement et de recherche français ou étrangers, des laboratoires publics ou privés.

Diagenetic formation of uranium-silica polymers in lake sediments over 3,300 years

Pierre Lefebvre[a,1], Alkiviadis Gourgiotis[b], Arnaud Mangeret[b], Pierre Sabatier[c], Pierre Le Pape[a], Olivier Diez[b], Pascale Louvat[d], Nicolas Menguy[a], Pauline Merrot[a,2], Camille Baya[a], Mathilde Zebracki[b], Pascale Blanchart[b], Emmanuel Malet[c], Didier Jézéquel[d,e], Jean-Louis Reyss[c], John R. Bargar[f], Jérôme Gaillardet[d], Charlotte Cazala[b], and Guillaume Morin[a]

[a]Institut de Minéralogie, de Physique des Matériaux et de Cosmochimie, UMR 7590 Sorbonne Université-CNRS-MNHN-IRD (Museum National d'Histoire Naturelle-Institut de Recherche pour le Développement), 75005 Paris, France; [b]Institut de Radioprotection et de Sûreté Nucléaire, PSE-ENV SEDRE, 92260 Fontenay-aux-Roses, France; [c]UMR 5204, Université Grenoble Alpes-Université Savoie Mont Blanc-CNRS-EDYTEM (Environnements DYnamiques et TErritoires de la Montagne), 73370 Le Bourget-Du-Lac, France; [d]UMR 7154, Université de Paris-Institut de Physique du Globe de Paris-CNRS, 75005 Paris, France; [e]INRAE-Université Savoie Mont Blanc, UMR CARRTEL (Centre Alpin de Recherche sur les Réseaux Trophiques et Ecosystèmes Limniques), 74200 Thonon-les-Bains, France; and [f]Stanford Synchrotron Radiation Lightsource, SLAC National Accelerator Laboratory, Menlo Park, CA 94025

Edited by François M. M. Morel, Princeton University, Princeton, NJ, and approved December 16, 2020 (received for review October 27, 2020)

The long-term fate of uranium-contaminated sediments, especially downstream former mining areas, is a widespread environmental challenge. Essential for their management is the proper understanding of uranium (U) immobilization mechanisms in reducing environments. In particular, the long-term behavior of noncrystalline U(IV) species and their possible evolution to more stable phases in subsurface conditions is poorly documented, which limits our ability to predict U long-term geochemical reactivity. Here, we report direct evidence for the evolution of U speciation over 3,300 y in naturally highly U-enriched sediments (350–760 $\mu g \cdot g^{-1}$ U) from Lake Nègre (Mercantour Massif, Mediterranean Alps, France) by combining U isotopic data ($\delta^{238}U$ and ($^{234}U/^{238}U$)) with U L_3-edge X-ray absorption fine structure spectroscopy. Constant isotopic ratios over the entire sediment core indicate stable U sources and accumulation modes, allowing for determination of the impact of aging on U speciation. We demonstrate that, after sediment deposition, mononuclear U(IV) species associated with organic matter transformed into authigenic polymeric U(IV)–silica species that might have partially converted to a nanocrystalline coffinite ($U^{IV}SiO_4{\cdot}nH_2O$)-like phase. This diagenetic transformation occurred in less than 700 y and is consistent with the high silica availability of sediments in which diatoms are abundant. It also yields consistency with laboratory studies that proposed the formation of colloidal polynuclear U(IV)–silica species, as precursors for coffinite formation. However, the incomplete transformation observed here only slightly reduces the potential lability of U, which could have important implications to evaluate the long-term management of U-contaminated sediments and, by extension, of U-bearing wastes in silica-rich subsurface environments.

uranium | noncrystalline species | diagenetic aging | lake sediments | uranium isotopes

Uranium (U) mining and milling activities since the mid-twentieth century have resulted in the contamination of freshwater bodies (1), such as on-site pit lakes (2) including in some non-U mining districts (3), as well as lakes and reservoirs downstream U mines (4–8). In these water bodies, the sediments accumulated U because of the development of anoxic conditions that are known to favor U reduction and immobilization as poorly soluble tetravalent U(IV) (9, 10). Predicting the long-term mobility of U under anoxic conditions is of major importance to implement reliable management methods, such as maintaining U-contaminated sediments under water or dredging and storing them aboveground. However, this prediction turns out to be challenging because of the diversity of reduced U(IV) chemical forms and the lack of related thermodynamic data to evaluate their stability (e.g., 11). Among these U forms, noncrystalline U(IV) species (also referred to as mononuclear U(IV)), often produced by microbial U(VI) reduction (12–18), have been recognized as a major U pool in reduced contaminated soils and sediments over the last decade (6, 7, 19–25) and are known to be sensitive to reoxidation by natural oxidants such as oxygen or nitrate (26 and references therein).

Even under reducing conditions, the long-term stability of non-crystalline U(IV) remains yet poorly constrained. Noncrystalline U(IV) was dominant both in recent (6) and decades-old sediments (7) of an artificial lake located downstream a former U mine in France. Residual uranium in the form of nanocrystalline U(IV)-phosphates was also observed in the deep sediments and their formation could not be elucidated despite a detailed spectroscopic and mineralogical analysis (7). Newsome et al. showed that noncrystalline U(IV) partially transformed to nano-uraninite (UO_2) after 15 mo of aging in laboratory (18). On the opposite, incubated bio-reduced sediments containing monomeric U(IV) did not show any transformation after 1 y (17, 27). Noncrystalline U(IV) was reported in contaminated floodplain sediments (23, 24, 28) and wetlands (19, 20, 22, 25) variably

Significance

Understanding the long-term fate of widespread noncrystalline uranium (U) species is critical to improving our knowledge of U biogeochemistry and U-contaminated environments. We use naturally U-enriched lake sediments that have been deposited for thousands of years as an analogue for the progressive evolution of contaminated environments, in order to uncover if noncrystalline species may evolve into more resistant crystalline phases. We combine multidisciplinary tools including U isotope ratio and speciation techniques to describe a mineralogical transformation where organic-bound U evolves into polymeric and nanocrystalline uranium-silica phases that are still easily remobilized even 3,300 y after their deposition. These findings bring an interpretation that illuminates an active debate on uranium mobility in the environment.

Author contributions: P. Lefebvre, A.G., A.M., P.S., P.L.P., J.-L.R., J.R.B., J.G., C.C., and G.M. designed research; P. Lefebvre, A.G., A.M., P.S., P.L.P., O.D., P. Louvat, N.M., P.M., C.B., M.Z., P.B., E.M., D.J., and G.M. performed research; P. Lefebvre, A.G., A.M., P.S., P.L.P., and G.M. analyzed data; and P. Lefebvre, A.G., A.M., P.S., P.L.P., and G.M. wrote the paper.

The authors declare no competing interest.

This article is a PNAS Direct Submission.

Published under the PNAS license.

[1]To whom correspondence may be addressed. Email: pierre.lefebvre@sorbonne-universite.fr.

[2]Present address: Environnement et Paléoenvironnements Océaniques et Continentaux, UMR 5805 (LPTC Research Group), CNRS-Université de Bordeaux, 33400 Talence, France.

This article contains supporting information online at https://www.pnas.org/lookup/suppl/doi:10.1073/pnas.2021844118/-/DCSupplemental.

Published January 21, 2021.

Downloaded from https://www.pnas.org by 81.249.197.186 on March 15, 2023 from IP address 81.249.197.186.

submitted to redox fluctuations for decades and even after three million years in a roll-front U deposit (29). However, the exact age of these U species is undetermined as are the potential mineralogical transformations that could have affected U-bearing phases in these systems.

Here, we report the long-term evolution of uranium speciation over 3,300 y in exceptionally U-enriched sediments from a pristine Mediterranean alpine lake, Lake Nègre (Mercantour-Argentera Massif, France), providing a unique insight into the long-term behavior of noncrystalline U(IV) under permanent anoxia. Combining solid U speciation techniques (X-ray absorption spectroscopy) to high precision isotopic analyses (($^{234}U/^{238}U$) and $\delta^{238}U$), supported by electron microscopy observations, we provide direct evidence for diagenetic aging of noncrystalline U(IV) species in these natural lake sediments. In addition to the description of an original mineralogical transformation, our findings may have important implications for the understanding and long-term management of comparable U-contaminated sites, such as lacustrine sediments downstream U mines (2–8) and, to some extent, other anoxic environments such as aquifer sediments and peatlands (19–24, 30).

Results and Discussion

A Unique Naturally U-Enriched System. Lake Nègre is an oligotrophic 10-ha-wide lake located in a high-altitude (2,354 m above sea level), granitic catchment devoid of substantial vegetation (*SI Appendix*, Fig. S1), formed after the last deglaciation more than 11,000 y ago (31). The 28-m-deep water column is stratified in summer and oxygenated (*SI Appendix*, Fig. S2); sediments are anoxic below 2 mm (*SI Appendix*, Fig. S2). Due to low erosion rates, sediments are mainly constituted of biogenic deposits (particularly diatoms and organic matter) with a small detrital fraction (32). Two sediment cores were sampled in the central part of the lake and preserved under anoxic conditions according to proven protocols (6, 7): a main 198-cm-long core (NEG18-07) dedicated to sediment analysis, and a 110-cm-long core (NEG18-04) used to extract pore waters in the field in an anoxic glove bag. All solid-state data presented below were measured on core NEG18-07.

The cores are composed of three units from top to bottom (*SI Appendix*, Fig. S3): Unit T (*Top*, 0–4.5 cm), corresponding to loose clayey-silty sediments deposited since 1966 (dated by $^{210}Pb_{ex}$ geochronology (*SI Appendix*, Fig. S3)); Unit S (4.5 to 170.8 cm), composed of instantaneous mass wasted deposit due to seismic shots in the northern part of the lake in 1958 and 1966 (33); Unit B (*Bottom*, 170.8 to 198 cm), corresponding to compacted silty sediments, radiocarbon-dated from −15 cal B.P. (1965 AD) to 3,230 cal B.P. (*SI Appendix*, Fig. S3 and Table S1). The pristine Units T and B of core NEG18-07 were selected to study U solid-state speciation and early diagenesis. Age–depth modeling results in apparent sediment accumulation rates of 0.69 $mm.y^{-1}$ and 0.08 $mm.y^{-1}$ in Unit T and B respectively, the difference being explained by compaction of the deep unit and by the high water content of the upper sediments. Powder X-ray diffraction (XRD) analyses (*SI Appendix*, Fig. S6) show a larger fraction of detrital granitic minerals (quartz, feldspars, and clays) in Unit T than in Unit B. Besides, a high amorphous silica content (*SI Appendix*, Fig. S6) related to abundant diatom tests (*SI Appendix*, Fig. S7) is observed in Unit B despite a slightly lower average SiO_2 content than in Unit T (58.0 ± 2.2 and 61.8 ± 1.7 wt%, respectively).

Uranium and total organic carbon (TOC) contents progressively increase with depth along Units T and B, from 350 to 760 $\mu g \cdot g^{-1}$ and from 5.2 to 12.1 wt%, respectively (Fig. 1 *A* and 1*B*), with a good correlation ($R^2 = 0.94$, $P < 0.005$) (*SI Appendix*, Fig. S9). Such U contents in natural lake sediments are exceptionally high compared to the typical range of 0.5 to 5 $\mu g.g^{-1}$ (34), especially in an oxygenated water setting (e.g., 35). They are two orders of magnitude higher than the U content in the watershed background rocks (3.6 ± 2.7 $\mu g.g^{-1}$, $n = 6$) and thus indicate a remarkable enrichment process, with U concentrations similar to that of U tailings (1). Variations of the accumulated TOC amounts may be linked to climate-induced changes in terrigenous and autochthonous organic matter productivity over

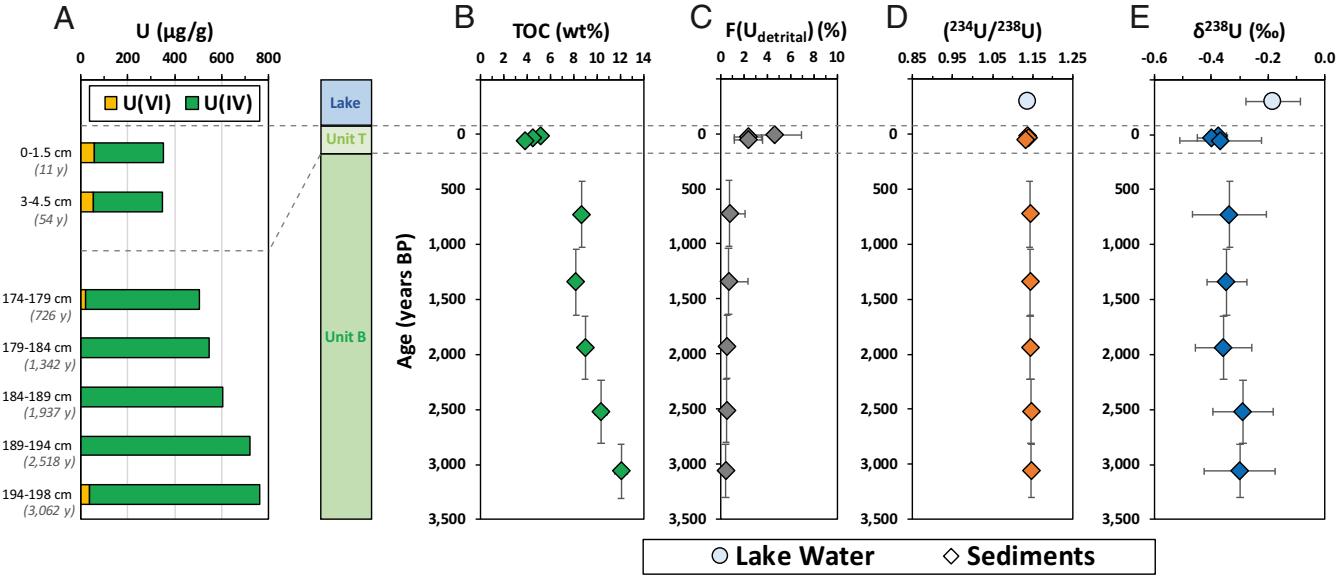

Fig. 1. (*A*) U concentration and redox state (U(VI) and U(IV) proportions from U L_3-edge XANES spectroscopy) with 0–1.5 and 3–4.5 cm samples from Unit T and 174 to 198-cm samples from Unit B (with ages in years B.P.). Bottom core U(VI) proportions are within the typical uncertainty of 5 to 10% for XANES redox determination. (*B*) TOC content in sediments along Units T and B of core NEG18-07. (*C*) Detrital U fraction (% of the total U pool) calculated from U/Th ratios. Isotopic signatures ($^{234}U/^{238}U$) (*D*) and $\delta^{238}U$ (*E*) of the lake inlet water (circle) and sediments along core NEG18-07 (diamonds). Vertical error bars indicate age intervals; horizontal error bars correspond to 2SD uncertainties.

Downloaded from https://www.pnas.org by 81.249.197.186 on March 15, 2023 from IP address 81.249.197.186.

the last 3,300 y, as documented in other alpine lakes in similar contexts (e.g., 36, 37).

In order to investigate U sources, we measured the aqueous U concentration at the spring of the main stream of the watershed (northeast of the lake) and found a bulk (nonfiltered) U concentration of 12.6 ± 0.5 $\mu g.L^{-1}$. This stream crosses a wetland before reaching the lake, which contains U at 2.6 ± 0.1 $\mu g.L^{-1}$ 20 m from the lake inlet. Sequential ultrafiltration of the lake water showed that U is transported by colloids (<0.2 μm) of varying sizes (*SI Appendix*, Fig. S10) that are thought to be mostly organic and mineral compounds released from the watershed soils and the wetland. In our case, U sources to the sediments are represented by the lake inlet water.

Assessing U Sources and Depositional Processes. In the aim of assessing the long-term evolution of U speciation after sediment deposition, it was necessary to ensure that U transport and depositional processes remained comparable over the last 3,300 y. For this reason, high precision uranium isotope ratios ($^{234}U/^{238}U$) and $^{238}U/^{235}U$ (expressed as $\delta^{238}U$) were used as a fingerprint of U sources as well as of the processes leading to U deposition in the sediments (38, 39, and references therein). The ($^{234}U/^{238}U$) activity ratios of the sediments, lake inlet water, and spring fall within the same range of values (1.141 ± 0.011, 1.136 ± 0.012, and 1.155 ± 0.009, respectively) that are consistent with the weathering of background rocks (38, 40) (Fig. 1*D*). Stable ratios along the core indicate that U has been constantly supplied by bedrock weathering for the last 3,300 y.

Since thorium (Th) compounds are far less soluble than U ones in oxic environments, $^{238}U/^{232}Th$ ratios can be used to assess the detrital U fraction (i.e., hosted by primary U minerals) (41–43). Using mixing equations for interpreting $^{238}U/^{232}Th$ ratios, we found that Unit T—recent sediments—contains 3.1 ± 2.6% detrital U, while the detrital U fraction of deep Unit B sediments decreases with depth from 0.7 to 0.4% of total U (Fig. 1*C* and *SI Appendix*, Fig. S11). Hence, the fraction of detrital U, likely hosted by granitic minerals such as zircons and monazite as observed by scanning electron microscopy coupled with energy-dispersive X-ray spectroscopy (*SI Appendix*, Fig. S7), slightly increased in time (which may be explained by lower dilution by organic matter) but remained below 5% of total U in the sediments. Thorough examination of Unit B samples by scanning transmission electron microscopy (STEM-EDXS) allowed us to detect trace U dispersed in the sediment matrix (*SI Appendix*, Figs. S12–S15) and a single U-bearing particle (~80 nm) (*SI Appendix*, Fig. S15).

The $\delta^{238}U$ isotope signature of the upper 3 cm of sediments (−0.38 ± 0.06‰) is slightly lower than that of the lake inlet water (−0.18 ± 0.10‰) (Fig. 1*E*). The relative behavior of ^{235}U and ^{238}U (expressed by $\delta^{238}U$) has been described for most chemical reactions (see the review by 39), suggesting that the dominant mechanism here is adsorption of U to colloidal biomass or minerals within the water column (44), and excluding U enrichment in the sediments by diffusion followed by reduction at the sediment–water interface, that would have induced a positive isotopic fractionation (5, 45, 46). Consequently, since U is correlated to organic carbon (*SI Appendix*, Fig. S9) and is mostly nondetrital (Fig. 1*C*) in the sediments, we conclude that U accumulation is driven by U binding to lacustrine biomass or terrigenous organic colloids followed by sedimentation (47). More importantly, the constant $\delta^{238}U$ over the entire core (average −0.34 ± 0.08‰, Fig. 1*E*) tends to show that U deposition processes remained similar over the 3,300-y period.

Overall, our isotopic analyses show that U sources and U transport and deposition processes in Lake Nègre sediments remained comparable in nature—if not in amplitude—over the studied period, allowing us to evaluate the sole effects of diagenetic aging on U solid speciation. The observed decrease in U concentrations over age may have been caused by lowering lacustrine and/or terrigenous organic matter (OM) production or dilution by concomitantly increasing terrigenous inputs.

Evolution of Uranium Speciation in the Sediments. The redox state and speciation of U was determined by synchrotron-based X-ray absorption spectroscopy (XAS) at the U L_3-edge. X-ray absorption near-edge structure (XANES) analysis shows that U is readily reduced in the sediments: 84 ± 3% of U is present as U(IV) at 0–1.5 cm (Fig. 1*A* and *SI Appendix*, Table S2 and Fig. S16), as compared to 30 to 50% U(IV) at the same depth in anoxic lacustrine sediments with similar TOC (6). Complete reduction occurs at depth in Unit B with U(IV) proportions ranging between 95 and 100% (Fig. 1*A* and *SI Appendix*, Table S2 and Fig. S16), concomitant with the presence of framboidal pyrite in Unit B only (*SI Appendix*, Fig. S8). Uranium(VI) reduction might be favored by the high TOC content and anoxia below 2 mm (*SI Appendix*, Fig. S2), which may stimulate the activity of dissimilatory metal- and sulfate-reducing bacteria (48–50). The mechanism of U reduction might then involve biotic and abiotic pathways in variable contributions, via direct or indirect electron transfer (6, 27, 48–50). The absence of any significant isotopic variation within the sediments indicates that most U was likely adsorbed before being reduced (51, 52).

The region of the extended X-ray absorption fine structure (EXAFS) between 2 to 7.5 $Å^{-1}$ is dominated by signal from the oxygen coordination shell of U, which is well modeled using eight neighboring O atoms (Fig. 2 and Table 1 and *SI Appendix*, Fig. S17 and Table S3). In contrast, the spectral region between 7.5 and 13 $Å^{-1}$ is substantially influenced by backscattering from higher-Z elements (Si, P, and U), which here correspond to second neighbors of U at ≥ 3 Å. The sharp contrasts in peak (and valley) intensities and positions starting at 7.5 $Å^{-1}$ indicate corresponding important differences in these second neighbor shells as a function of sediment age. More precisely, shell-by-shell analysis of the EXAFS spectra shows that U is deposited as noncrystalline/mononuclear U in the recent Unit T sediments, with ~2.4 monodentate C neighbors at 3.54 Å, two distances of Si or P neighbors at 3.12 Å (n = 1.1, edge-sharing linkage) and 4.0 Å (n = 1.0, corner-sharing, enhanced by U-O-Si-O or U-O-P-O multiple scattering) and no observable U neighbor (Fig. 2 and Table 1 and *SI Appendix*, Fig. S20 and Table S5). This finding is in accordance with U adsorption to terrigenous organic matter and/or to primary biomass and diatoms tests, which reinforces the geochemical evidence for U binding to organic-rich colloidal material in the water column, as proposed in the previous section.

In contrast, in the deep sediments of Unit B, no organic (C) neighbors were identified despite the low proportion of detrital U. Instead, we observe a net increase in the contributions of Si atoms at 3.1 Å (n = 2, edge-sharing) and 4.0 Å (n = 2.3, corner-sharing) together with a clear contribution of long-distance heavy atom neighbors, well fitted by 0.8 U atom at 3.98 Å (Table 1). These contributions to the EXAFS are respectively shown by the rising peaks at 2.5 and 4 Å (uncorrected for phase-shift) in the fast Fourier transforms (Fig. 2 and *SI Appendix*, Fig. S17). This change in the local environment of U is also particularly illustrated by continuous Cauchy wavelet transform (CCWT) analysis (Fig. 2 and Table 1), as detailed in the *SI Appendix*. This particular set of distances matches that of the coffinite ($U^{IV}SiO_4 \cdot nH_2O$) structure, albeit with a lower number of long-distance Si and U neighbors (Table 1), suggesting that U is mainly present in the form of coffinite-like U(IV)-silica polymers or nanocrystalline coffinite. Although the short U–Si distance is well defined and exactly matches that in coffinite at 3.1 Å, a slightly longer U–Si/U distance (4.0 Å) is observed compared to crystalline coffinite (3.83 Å), as discussed in the *SI Appendix*. The identification of Si neighbors rather than commonly found P neighbors

Downloaded from https://www.pnas.org by 81.249.197.186 on March 15, 2023 from IP address 81.249.197.186.

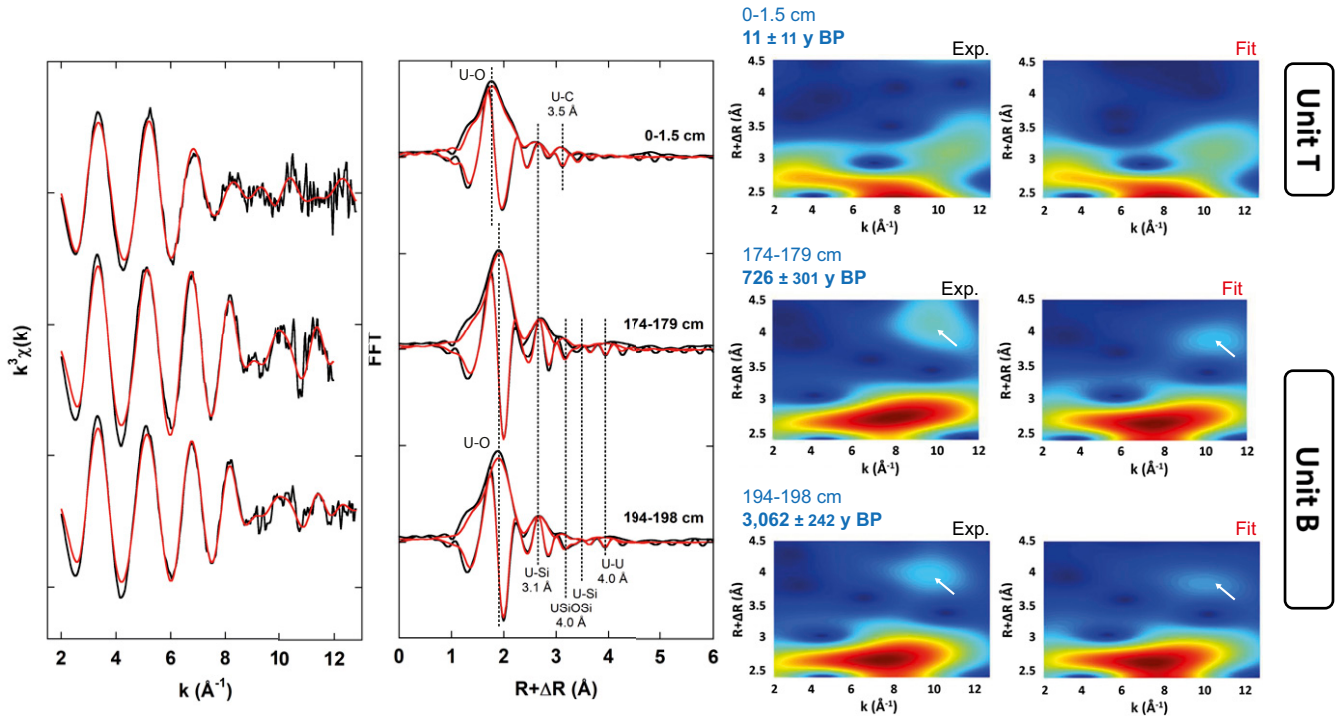

Fig. 2. Shell-by-shell fit of U L_3-edge EXAFS data over the 2 to 12.8 $Å^{-1}$ k-range for the uppermost Unit T sediment sample (0–1.5 cm) and the deepest sample of Unit B (194–198 cm), and over the 2 to 12 $Å^{-1}$ k-range for the uppermost Unit B sample (174–179 cm). (*Left*) Fitting of the unfiltered k^3-weighted EXAFS data in k-space. (*Middle*) Fast Fourier Transform (FFT) of the experimental and fit curves. Fitting parameters are reported in Table 1. Experimental and fit curves are displayed as black and red color, respectively. The first main peak at ~2 Å (uncorrected for phase shift) on the FFT curves corresponds to the U–O shells. (*Right*) CCWT of the experimental (Exp.) and fitted (Fit) EXAFS data. The peak at k~10 $Å^{-1}$ and R~4 Å in the CCWT amplitude map (indicated by a white arrow) supports the presence of a U–U pair at 4.0 Å in Unit B samples, as indicated also in the FFT curves above.

in non-crystalline U(IV) species is fueled here by two observations: 1) the fits with Si neighbors are better than with P neighbors, both visually (*SI Appendix*, Fig. S19) and statistically (*SI Appendix*, Table S4), and 2) either with P or Si, the fits are better with interatomic distances close to those in coffinite (Table 1), rather than those in U(IV) phosphates such as U-rhabdophane/ningyoite (ref. 7 and references therein). Significant U incorporation into zircons is excluded since U is mostly nondetrital. This U speciation, consistently observed over five samples covering average time periods from 730 to 3,060 y B.P. (*SI Appendix*, Figs. S17 and S18 and Table S3), could result from diagenetic reprecipitation of U. The sediment pore waters contain high dissolved Si concentrations (18.3 to 26.3 $mg.L^{-1}$) together with dissolved U from 2.6 to 4.3 $\mu g.L^{-1}$ (*SI Appendix*, Fig. S21). Thermodynamic calculations (*SI Appendix*) showed that, in the pore waters conditions, the precipitation of crystalline UO_2, ningyoite ($CaU(PO_4)_2{\cdot}2H_2O$), and coffinite ($USiO_4{\cdot}nH_2O$) are favorable, while amorphous uraninite and coffinite should be at equilibrium with the solution (53–56). As shown by bulk EXAFS analysis, U mainly binds to silica in the deep sediment layers, indicating that, although they cannot be excluded, uraninite or U-phosphate mineral species are likely minor in these samples. We hypothesize that the presence of silicate moieties inhibited the precipitation of uraninite (12, 13, 16, 57) and favored the polymerization of coffinite-like phases. One should keep in mind that the observed speciation is an average picture of U mineralogy in the sediments. Local heterogeneities of the sediment components (e.g., ligands and electron donors) may have induced heterogeneities in uranium phases, for instance with minor phases of phosphate-bound U(IV) or nanouraninite that cannot be detected by bulk EXAFS. Indeed, it has been shown that U immobilization mechanisms may vary depending on the environmental conditions, particularly the availability of ligands and electron donors (58). Here, the mechanism of the observed transformation may imply either uranium dissolution and reprecipitation through potential reoxidation or solid-state reorganization of U(IV) monomers to polymeric species. However, unveiling such detailed pathways would require controlled experiments, such as that of Bargar et al. (27), that are unachievable over time scales of hundreds to thousands of years.

The observed change in U speciation was quantified by chemical extraction with 1 M ($mol.L^{-1}$) $NaHCO_3$ that remobilizes noncrystalline U, including polymeric species (59). Results show that 78 ± 3% of U in deep sediments is easily HCO_3^--mobilized by comparison with 83 ± 1% in the top-layer sediments (Fig. 3 and *SI Appendix*, Fig. S22). Hence, taking into account the small proportion of detrital U (Fig. 1*C*), the fraction of bicarbonate-resistant nondetrital U(IV) slightly increases from 14 ± 4% in the most recent sediments to an average of 22 ± 3% in the oldest sediments (Fig. 3 and *SI Appendix*, Fig. S22). This nonextractable fraction of U(IV) may be attributed to a nanocrystalline coffinite phase or to a U(IV)–silicate amorphous phase in which the individual U monomers are sufficiently polymerized to prevent dissolution by bicarbonate. Although the sodium bicarbonate extraction results suggest that such phases may already be present in the recent sediments (Fig. 3), their proportion (~14%) is typically too low to be conclusively demonstrated by EXAFS. In contrast, in the oldest sediments, an increase in U(IV) binding to silica and a significant polymerization of U(IV)–silica species allows these phases to be clearly observed by EXAFS (Fig. 2). However, this transformation of U speciation seems to only slightly decrease the solubility of the U(IV) phases. This level of reactivity suggests that a continuum of U(IV)–silica species, from mononuclear to polymeric U(IV), is present. The degree of polymerization increases during diagenesis, to ultimately mimic the local structure of nano-coffinite.

Downloaded from https://www.pnas.org by 81.249.197.186 on March 15, 2023 from IP address 81.249.197.186.

Table 1. Uranium crystal structure parameters in sediments compared to coffinite

Sample depth, age, and k-range	Path	R (Å)	CN	σ (Å)	ΔE_0 (eV)	χ^2_R
0–1.5 cm	U–O	1.78*	0.26 (6)	0.081 (2)	−1.2 (6)	3.5
11 ± 11 years BP	U–O	2.313(4)	4*	—	—	
k 2–12.8 $Å^{-1}$	U–O	2.479(5)	4*	—	—	
	U–Si	3.117(7)	1.1 (3)	—	—	
	U–Si	4.00*	1.0 (8)	—	—	
	U–Si–O–Si	4.00*	—	—	—	
	U–C	3.54(2)	2.4 (7)	—	—	
174–179 cm	U–O	1.78*	0.28 (7)	0.076 (2)	−0.2 (7)	7.2
726 ± 301 years BP	U–O	2.365(5)	4*	—	—	
k 2–12 $Å^{-1}$	U–O	2.489(7)	4*	—	—	
	U–Si	3.144(6)	2*	—	—	
	U–Si	4.00*	3.3 (11)	—	—	
	U–Si–O–Si	4.00*	—	—	—	
	U–U	3.98*	0.8 (2)	—	—	
194–198 cm	U–O	1.78*	0.35 (12)	0.087 (7)	−0.2 (10)	12.2
3,062 ± 242 years BP	U–O	2.361(8)	4*	—	—	
k 2–12.8 $Å^{-1}$	U–O	2.49(1)	4*	—	—	
	U–Si	3.13 (1)	2*	—	—	
	U–Si	4.00*	2.3 (17)	—	—	
	U–Si–O–Si	4.00*	—	—	—	
	U–U	3.98*	0.8 (4)	—	—	
Coffinite crystal structure†,‡	U–O	2.29†–2.32‡	4			
	U–O	2.44†–2.52‡	4			
	U–Si	3.13†,‡	2			
	U–Si	3.83†,‡	4			
	U–U	3.83†,‡	4			

Results of U L_3-edge EXAFS shell-by-shell fitting for the uppermost Unit T sediment sample (0–1.5 cm) as well as uppermost (174–179 cm) and deepest (194–198 cm) samples of Unit B from core NEG18-07, over the 2 to 12.8 $Å^{-1}$ k-range (samples 0–1.5 cm and 194–198 cm) and over the 2 to 12 $Å^{-1}$ k-range (sample 174–179 cm). Coffinite crystal structure parameters were taken from ref. 93 and ref. 88. Corresponding curves are displayed in Fig. 2. Uncertainties on the last digit of each fitting parameter are given under bracket to 95% confidence, and fit quality is estimated by a reduced χ^2 (χ^2_R). R = path distance; CN = coordination number; σ = Debye–Waller factor; ΔE_0 = energy shift. "—" indicates the parameter is linked to the free parameter reported above in the table.
*Fixed parameter.
†Coffinite crystal structure parameters taken from ref. 93.
‡Coffinite crystal structure parameters taken from ref. 88.

In the oldest sediments, the proportion of bicarbonate-resistant phases interpreted as polymeric or nanocrystalline coffinite nevertheless remains around 22% of total U, which explains the observation of homogeneously dispersed U by STEM and of only one U-rich particle. Importantly, the observed diagenetic transformation of U does not appear to result in any resolvable (i.e., > 0.2‰) isotopic fractionation (*SI Appendix*, Fig. S24).

In naturally U-rich sediments of Lake Nègre, noncrystalline U(IV) was, therefore, transformed into a polymeric/nanocrystalline U(IV) coffinite-like phase after less than 730 y, showing a substantial effect of diagenesis in anoxic conditions on U species (Fig. 3). This newly formed U(IV) species then persisted over more than 2,300 y. Although it is present at most under nanocrystalline form, this is to our knowledge the first occurrence of a coffinite-like phase formation in nature at such low temperature (~5 °C) (60–62). Interestingly, this transformation was somehow predicted by a laboratory study that showed the formation of U(IV)–silica colloids in environmentally relevant conditions (63). It should be noted that the observed reaction is different from coffinitization that occurs at higher temperature through alteration of UO_{2+x} by Si-rich fluids (64). The present study thus underlines the growing role of naturally abundant silicate ligands to U coordination after long-term aging in low-temperature anoxic U-rich systems, in contrast with commonly reported biomass-bound phosphate and C ligands. Discriminating between these light neighboring atoms is difficult when dealing with mononuclear U species at trace level in environmental samples. We show for U-rich (350–760 $\mu g \cdot g^{-1}$) natural sediments that U L_3-edge EXAFS data to a k-value of 12.8 $Å^{-1}$—positively complemented by wavelet transform analysis—are conclusive to distinguish between silicate and other ligands.

Our results provide a long-term prediction for the fate of organic- and silica-rich U-contaminated systems, such as soils and freshwater sediments, where diatoms are widespread, and are of crucial importance for their management. To this regard, we show that long-term aging leads to polymerization of U(IV) and silica but only to incomplete recrystallization into nanocoffinite, which does not dramatically improve U scavenging efficiency, as measured by bicarbonate extraction. This result may be of importance for better constraining the long-term geochemical modeling of U-contaminated sediments in which the knowledge of reliable kinetics parameters for mineral formation at low-temperature is often limiting. The persistence of noncrystalline U(IV) species over millennial time scales, although they may transform into polymeric species, echoes that of ref. 18, albeit with different transformation products and on a much longer timescale. Additionally, the kinetics observed here explain the absence of transformation in laboratory experiments mimicking

Downloaded from https://www.pnas.org by 81.249.197.186 on March 15, 2023 from IP address 81.249.197.186.

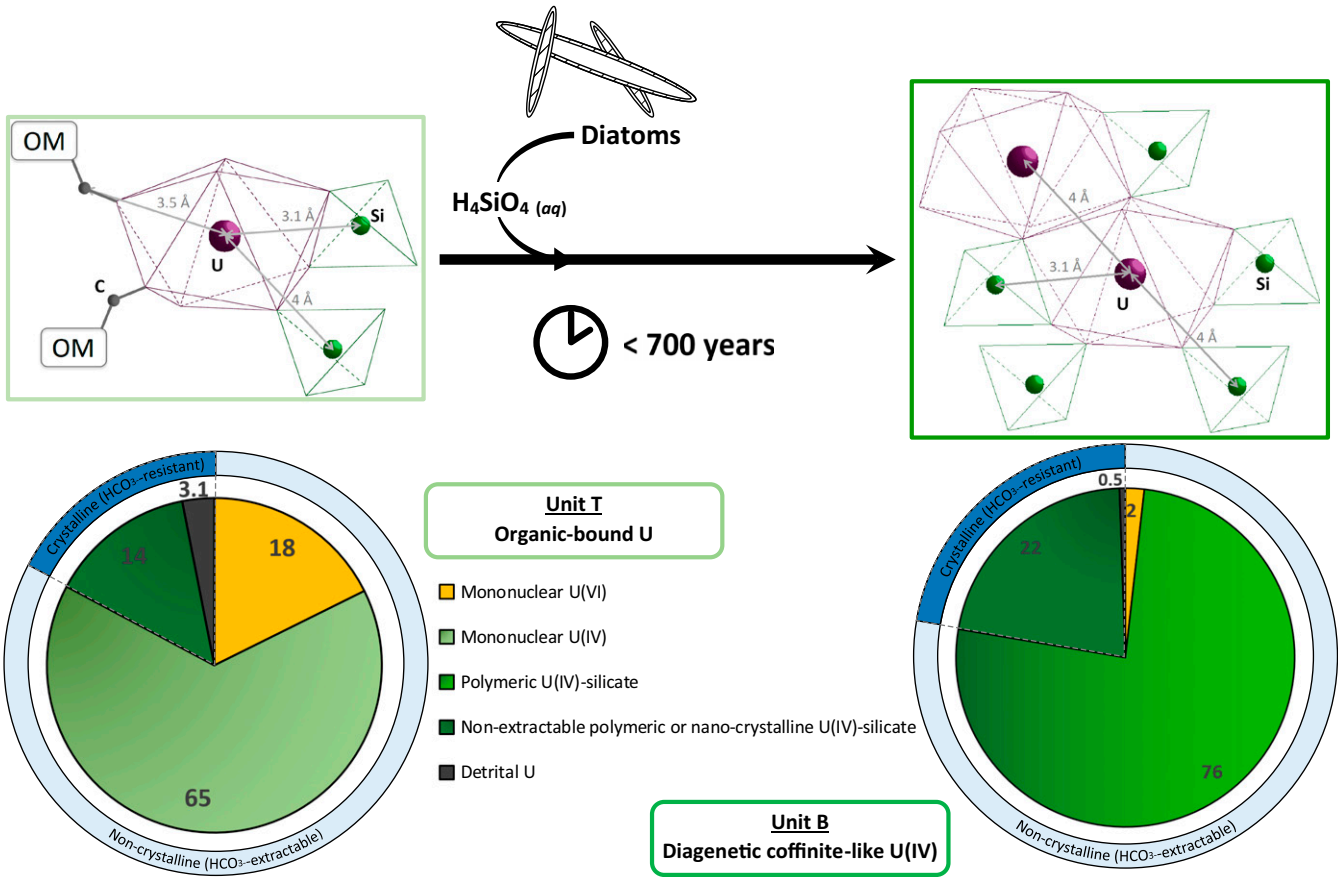

Fig. 3. Conceptual model of the observed natural U transformation: Noncrystalline U(IV) (Unit T, *Left*) transforms to U(IV)–silica polymers/nanocrystalline coffinite ($U^{IV}SiO_4.nH_2O$) (Unit B, *Right*) in less than 700 y in Lake Nègre sediments. This transformation is enhanced by diagenetic remobilization of Si, potentially from diatoms. Tentative models of molecular structure around U in the investigated samples are shown in boxes on the top; U atoms are represented in purple and Si (and/or P in Unit T) atoms in green; "OM" indicates organic matter-bound monodentate C neighbors (in gray). Coordination polyhedra to first oxygen ligands are drawn as thin lines. For Unit T, corner linkage to organic carbon (3.5 Å) in addition to U–Si and/or U-P contributions. For Unit B, short-range coffinite-like cluster with U–Si edge-sharing linkage (~3.1 Å) and slightly elongated distances (~4 Å) for edge-sharing U–U and corner-sharing U–Si linkage. Pie charts display resulting repartitions of crystalline and noncrystalline U fractions according to 1 M bicarbonate extraction (*SI Appendix, Supplementary Text* and Fig. S23), with uncertainties (2SD) between 3 and 4%. Gradation in the green color indicates an increase in the degree of polymerization of U(IV)–silica species.

environmental conditions over 1 y (17, 27). Such long-term persistence of noncrystalline U(IV) species in subsurface sediments reinforces the need for preserving sustainable anoxic conditions with a long-term perspective, and, assuming that polymeric species may be of colloidal size, attention has to be paid to evaluating the potential of such species to migrate under anoxic conditions (19).

Another major result of this study is the absence of detectable UO_2. It is now well documented that the previous assumption that UO_2 was the dominant product of U(VI) reduction in low-temperature subsurface environments should be reevaluated. Only a few studies that characterized U speciation in natural low-temperature environments actually reported occurrences of crystalline U(IV), and a fortiori UO_2, for alluvial sediments exposed to seasonal redox cycling (23, 24, 28), or subjected to laboratory incubation or biostimulation (18, 21, 27, 65, 66). In contrast, a majority of natural environments do not exhibit UO_2, such as recent lake sediments (6, 7), U-contaminated organic-rich wetlands (19, 20, 22, 25, 30), or other biostimulated soils and sediments (17, 69–72). In the light of these observations, the present study supports that the formation of uraninite is inhibited by the presence of aqueous and solid-associated ligands (e.g., organic matter–bound phosphoryl and carboxyl groups, and mineral phosphate and silicate ligands) that immobilize U(IV) under noncrystalline forms (12, 13, 16, 57, 67). The formation of nano-uraninite at low-temperature may be favored only when low concentrations of ligands are available compared to U(IV) concentration (16, 27, 67), which may be the case when redox cycles lead to exceptional accumulation of U(IV) in water-table fluctuations zones of aquifer sediments (23, 24, 28, 68).

Beyond these environmental perspectives, our results may also help to understand the preservation of U geochemical and isotopic signals that are used for paleo-redox studies in continental and marine sediments such as black shales (e.g., 45, 46). In these systems, solid U(IV) products are often either overlooked (45, 46) or considered as being uraninite by simplification (73). Considering the diversity of U(VI) reduction products that involve various chemical pathways—with potentially different isotope fractionation factors—the interpretation of U isotopes could thus benefit from the combined determination of U solid-state speciation.

Materials and Methods

Sampling. Sediment cores were sampled at the deepest point of Lake Nègre using an Uwitec gravity corer (63 mm in diameter) equipped with a hammer, then immediately closed under N_2 flux and further opened inside an anaerobic glovebox (<3 ppm O_2) at the Institut de Minéralogie, de Physique des Matériaux et de Cosmochimie (IMPMC) in order to preserve the redox state of the sediments. Subsamples from core NEG18-07 were homogenized and dried under vacuum within 48 h. All samples were stored in anoxic butyl rubber-sealed serum vials until analysis. Pore waters from core NEG18-04

Downloaded from https://www.pnas.org by 81.249.197.186 on March 15, 2023 from IP address 81.249.197.186.

were sampled in the field inside a N_2-purged glove bag by inserting Rhizon moisture samplers in predrilled holes every 4 cm along the core tube. Lake water was vacuum filtered in the field using a Sartorius filtration unit (0.2 and 0.01 μm cellulose filters) then ultrafiltered with an Amicon ultrafiltration cell (100 and 1 kDa regenerated cellulose filters). Filtrates were acidified with 68% ultra-pure distilled HNO_3.

Geochronology. Terrestrial plant macroremains were sampled at five depths on core NEG18-07 and radiocarbon dated by accelerator mass spectrometry at the Poznań Radiocarbon Laboratory (Poland). Radio elements were measured at the Institut de Radioprotection et de Sûreté Nucléaire (IRSN) by gamma spectrometry following protocols described in ref. 74. $^{210}Pb_{ex}$ was calculated by subtracting ^{226}Ra to total ^{210}Pb activities, and corresponding dates obtained using the Constant Flux: Constant Sedimentation (CF:CS) model (75) (*SI Appendix*, Fig. S3). Age–depth modeling of core NEG18-07 was done using the *R* software package "clam" (76) (*R* version 3.6.2, ref. 77) with $^{210}Pb_{ex}$ derived ages and radiocarbon dates (*SI Appendix*, Fig. S3 and Table S1). The chronology of core NEG18-04 was established by high-resolution X-ray fluorescence (XRF) correlation, specifically by fitting observable Pb historical pollution peaks (36, 78) (*SI Appendix*, Fig. S4 and Table S1).

Electron Microscopy. SEM data acquisition was performed at IMPMC using a Zeiss Ultra 55 microscope equipped with a field emission gun. EDXS data and back-scattered electron images were collected with a 15 kV emission at a working distance of 7.5 mm. EDXS data intensity was calibrated using the Cu K_α emission line of a Cu tape. Scanning transmission electron microscope high-angle annual dark-field imaging (STEM-HAADF) and STEM-EDXS elemental mapping was carried out on a Jeol 2100F microscope installed at IMPMC. This machine, operating at 200 kV, is equipped with a field emission gun, a high-resolution pole piece, and an ultrathin window Jeol detector.

Chemical Analyses. High-resolution (2 mm/step) elemental composition was measured on half-cores with an Avaatech XRF core-scanner at EDYTEM. Two tubes settings were used: 10 kV and 0.175 mA for 15 s for light elements and 30 kV and 0.245 mA for 35 s for heavy elements (79). Major elements were determined at the Service d'Analyze des Roches et Minéraux (SARM-CRPG, Nancy, France) by optical emission spectrometry (ICP-OES) after $LiBO_2$ alkali fusion. Subsamples of core NEG18-07 were digested with a mix of concentrated HNO_3 and HF at 90 °C for 24 h followed by addition of concentrated $HClO_4$ for 24 h, then heated to dryness at 160 °C and further dissolved in 2% HNO_3 for analysis. Trace elements were measured at the LUTECE laboratory (Laboratoire Unifié d'expérimenTation Et de CaractErisation, IRSN) with a triple quadrupole inductively coupled plasma mass spectrometer (ICP-MS/MS, Agilent 8800). TOC was determined using a carbon analyzer (Vario TOC Elementar) following the method described in ref. 6. All solid concentrations are expressed relative to sediment dry weight. Pore water major elements were analyzed with an inductively coupled plasma atomic emission spectrometer (ICP-AES, ICAP 7600 DUO ThermoFisher) at LUTECE.

Isotopic Analyses. Selected samples were double spiked with IRMM-3636a standard with a spike/sample ratio ($^{236}U/^{235}U$) of ~2 to 3 to correct from analytical and instrumental mass biases. The uranium fractions were extracted via column chromatography with UTEVA (Uranium and TEtraValent Actinides) resin (Eichrom Technologies, LLC), following a protocol adapted from ref. 80. Isotopic measurements were performed on a Thermo Finnigan Neptune Multi-Collector Inductively Coupled Plasma Mass Spectrometer (MC-ICP-MS) at the PARI platform (Institut de Physique du Globe de Paris [IPGP]). The measured $^{238}U/^{235}U$ values were first calculated relative to the bracketing standard IRMM-184 (81). Final isotopic values $\delta^{238}U$ discussed in this study are expressed relative to the commonly used CRM-145 standard (82) after applying an offset of −1.10‰. Each $\delta^{238}U$ value is an average of 3 to 5 measurements. Uncertainties were calculated as two SDs (2SD) from the replicates. The method accuracy was tested by using three reference materials (BCR-2, AGV-2, and HU-1) that were processed with the samples and show a good agreement with values published elsewhere (*SI Appendix*). ($^{234}U/^{238}U$) activity ratios were obtained by multiplying $^{234}U/^{238}U$ isotope ratios by the ratio of radioactive decay constants. Analytical blanks were processed as well and show negligible U levels (< 0.2 ng).

X-ray Absorption Spectroscopy. U L_3-edge XAS spectra were collected on sample pellets carefully preserved from oxidation according to proven procedures (6, 7, 20, 71), as reported in the *SI Appendix*. Data were acquired in fluorescence detection mode at liquid-N_2 temperature on the high-flux multipole wiggler beamline 11-2 (Stanford Synchrotron Radiation Lightsource), using an Si(220) double crystal monochromator and a Canberra 100 elements Ge array detector, and at liquid He temperature on the high-flux undulator beamline P64 (Deutsches Elektronen-Synchrotron), equipped with a Si(111) double crystal monochromator and a Passivated Implanted Planar Silicon detector. Calibration of the incident beam energy was performed by measuring the *K*-edge transmission spectrum of an yttrium (Y) foil and setting its first inflection point to 17,038.0 eV. On beamline 11-2, dead-time correction was done using the SIXpack software (83). XAS data were merged, normalized, and background subtracted with the ATHENA software (84).

XANES spectra were analyzed by linear combination least-squares (LC-LS) fitting with a custom-built software using procedures detailed in refs. 6, 7, and 85. The best LC-LS fits to the sediments data were obtained using torbernite as U(VI) reference and sample NEG18-07 184–189 cm as U(IV) reference as detailed in the *SI Appendix*. Shell-by-shell fitting of the unfiltered U L_3-edge k^3-weighted EXAFS spectra was performed following procedures reported by refs. 6, 7, and 85, with a custom-built software based on Levenberg–Marquardt minimization algorithm and using the plane-wave EXAFS formalism (86). Electron backscattering phase and amplitude functions used in these fitting procedures were calculated for curved-wave with the FEFF8.1 code (87) from the crystal structures of coffinite (88), torbernite (89), and uranyl acetate dihydrate (90). Fit quality and uncertainties were estimated as detailed in the SI. In order to firmly identify the neighboring atoms around U, consistency between the experimental and fitted EXAFS spectra was also checked by comparing their CCWT (6, 7, 85, 91) that were calculated using the Matlab script by refs. 91 and 92. Molecular structure models in Fig. 3 and *SI Appendix*, Fig. S18 were represented with the CrystalMaker software. For a comparison of all EXAFS spectra, see *SI Appendix*, Figs. S17 and S18.

Bicarbonate Extractions. The noncrystalline U(IV) and U(VI) fractions of sediment samples were quantified by suspending ~300 mg dry sediment in 5 mL of 1 M $NaHCO_3$ solution for 100 h in the anaerobic glovebox following a protocol adapted from ref. 59.

For a detailed description of the full methods and additional data, please refer to *SI Appendix*. For additional data, please see Dataset S1.

Data Availability. All study data are included in the article and/or supporting information.

ACKNOWLEDGMENTS. We thank Gilles Alcalde and Cyrielle Jardin (IRSN); Jessica Brest, Ludovic Delbès, Arnaud Duverger, and Imène Esteve (IMPMC); Anne-Lise Develle (Environnements DYnamiques et TErritoires de la Montagne); and Barthélémy Julien (IPGP) for their help in chemical, XRD, STEM-EDX, SEM-EDX, XRF and MC-ICP-MS analyses, respectively. We greatly acknowledge the Parc National du Mercantour for having authorized access to and sampling in Lake Nègre. The authors are greatly indebted to Ryan Davis for his assistance during measurements at Stanford Synchrotron Radiation Lightsource (SSRL) beamline 11-2. We also thank Matthew Root and Marcia Torres for their assistance in sample management at SSRL. The SSRL, Stanford Linear Accelerator Center National Accelerator Laboratory, is a national user facility supported by the United States Department of Energy, Office of Science, and Office of Basic Energy Sciences under Contract No. DE-AC02-76SF00515. We acknowledge the France–Stanford program "International Collaboration for Mitigating Mine Wastes for Improved Groundwater" for travel support. Deutsches Elektronen-Synchrotron (Hamburg, Germany), a member of the Helmholtz Association of German Research Centres is acknowledged for the provision of experimental facilities and travel support. Parts of this research were carried out at PETRA III beamline P64 and we thank Wolfgang Caliebe for assistance during experiments. Parts of this work were supported by IPGP multidisciplinary program PARI and by Paris–IdF Region SESAME Grant no. 12015908. This study contributes to the IdEx Université de Paris ANR-18-IDEX-0001. This work was supported by IRSN through collaborative research program n° LS 20942, and by the Programme National EC2CO-BIOHEFECT/ECODYN (PUMA). This is PATERSON, the IRSN's mass spectrometry platform, contribution no. 8.

1. A. Abdelouas, Uranium mill tailings: Geochemistry, mineralogy, and environmental impact. *Elements* **2**, 335–341 (2006).
2. K. von Gunten *et al*., Colloidal transport mechanisms and sequestration of U, Ni, and As in meromictic mine pit lakes. *Geochim. Cosmochim. Acta* **265**, 292–312 (2019).
3. J. Mantero *et al*., Pit lakes from southern Sweden: Natural radioactivity and elementary characterization. *Sci. Rep.* **10**, 13712 (2020).
4. D. H. Dang, W. Wang, P. Pelletier, A. J. Poulain, R. D. Evans, Uranium dispersion from U tailings and mechanisms leading to U accumulation in sediments: Insights from biogeochemical and isotopic approaches. *Sci. Total Environ.* **610-611**, 880–891 (2018).
5. W. Wang, D. H. Dang, B. Novotnik, T. T. Phan, R. D. Evans, Variations in U concentrations and isotope signatures in two Canadian lakes impacted by U mining: A combination of anthropogenic and biogeochemical processes. *Chem. Geol.* **506**, 58–67 (2019).

Downloaded from https://www.pnas.org by 81.249.197.186 on March 15, 2023 from IP address 81.249.197.186.

6. L. Stetten *et al*., Geochemical control on the reduction of U(VI) to mononuclear U(IV) species in lacustrine sediments. *Geochim. Cosmochim. Acta* **222**, 171–186 (2018).
7. G. Morin *et al*., Mononuclear U(IV) complexes and ningyoite as major uranium species in lake sediments. *Geochem. Perspect. Lett.* **2**, 95–105 (2016).
8. S. R. Joshi, D. T. Waite, R. F. Platford, Vertical distribution of uranium mill tailings contaminants in Langley bay, Lake Athabasca sediments. *Sci. Total Environ.* **87–88**, 85–104 (1989).
9. D. Langmuir, Uranium solution-mineral equilibria at low temperatures with applications to sedimentary ore deposits. *Geochim. Cosmochim. Acta* **42**, 547–569 (1978).
10. K. Maher, J. R. Bargar, G. E. Brown Jr, Environmental speciation of actinides. *Inorg. Chem.* **52**, 3510–3532 (2013).
11. J. M. Cerrato *et al*., Relative reactivity of biogenic and chemogenic uraninite and biogenic noncrystalline U(IV). *Environ. Sci. Technol.* **47**, 9756–9763 (2013).
12. R. Bernier-Latmani *et al*., Non-uraninite products of microbial U(VI) reduction. *Environ. Sci. Technol.* **44**, 9456–9462 (2010).
13. M. I. Boyanov *et al*., Solution and microbial controls on the formation of reduced U(IV) species. *Environ. Sci. Technol.* **45**, 8336–8344 (2011).
14. D. S. Alessi *et al*., The product of microbial uranium reduction includes multiple species with U(IV)–phosphate coordination. *Geochim. Cosmochim. Acta* **131**, 115–127 (2014).
15. K. E. Fletcher *et al*., U(VI) reduction to mononuclear U(IV) by Desulfitobacterium species. *Environ. Sci. Technol.* **44**, 4705–4709 (2010).
16. M. Stylo *et al*., Biogeochemical controls on the product of microbial U(VI) reduction. *Environ. Sci. Technol.* **47**, 12351–12358 (2013).
17. L. Loreggian *et al*., Effect of aging on the stability of microbially reduced uranium in natural sediment. *Environ. Sci. Technol.* **54**, 613–620 (2020).
18. L. Newsome, K. Morris, S. Shaw, D. Trivedi, J. R. Lloyd, The stability of microbially reduced U(IV); impact of residual electron donor and sediment ageing. *Chem. Geol.* **409**, 125–135 (2015).
19. Y. Wang *et al*., Mobile uranium(IV)-bearing colloids in a mining-impacted wetland. *Nat. Commun.* **4**, 2942 (2013).
20. L. Stetten *et al*., Redox fluctuations and organic complexation govern uranium redistribution from U(IV)-phosphate minerals in a mining-polluted wetland soil, brittany, France. *Environ. Sci. Technol.* **52**, 13099–13109 (2018).
21. D. S. Alessi *et al*., Speciation and reactivity of uranium products formed during in situ bioremediation in a shallow alluvial aquifer. *Environ. Sci. Technol.* **48**, 12842–12850 (2014).
22. C. Mikutta, P. Langner, J. R. Bargar, R. Kretzschmar, Tetra- and hexavalent uranium forms bidentate-mononuclear complexes with particulate organic matter in a naturally uranium-enriched peatland. *Environ. Sci. Technol.* **50**, 10465–10475 (2016).
23. V. Noël *et al*., Redox controls over the stability of U(IV) in floodplains of the upper Colorado river basin. *Environ. Sci. Technol.* **51**, 10954–10964 (2017).
24. V. Noël, K. Boye, R. K. Kukkadapu, Q. Li, J. R. Bargar, Uranium storage mechanisms in wet-dry redox cycled sediments. *Water Res.* **152**, 251–263 (2019).
25. Y. Wang *et al*., Geochemical control on uranium(IV) mobility in a mining-impacted wetland. *Environ. Sci. Technol.* **48**, 10062–10070 (2014).
26. L. Newsome, K. Morris, J. R. Lloyd, The biogeochemistry and bioremediation of uranium and other priority radionuclides. *Chem. Geol.* **363**, 164–184 (2014).
27. J. R. Bargar *et al*., Uranium redox transition pathways in acetate-amended sediments. *Proc. Natl. Acad. Sci. U.S.A.* **110**, 4506–4511 (2013).
28. N. P. Qafoku *et al*., Geochemical and mineralogical investigation of uranium in multi-element contaminated, organic-rich subsurface sediment. *Appl. Geochem.* **42**, 77–85 (2014).
29. A. Bhattacharyya *et al*., Biogenic non-crystalline $U^{(IV)}$ revealed as major component in uranium ore deposits. *Nat. Commun.* **8**, 15538 (2017).
30. S. Regenspurg *et al*., Speciation of naturally-accumulated uranium in an organic-rich soil of an alpine region (Switzerland). *Geochim. Cosmochim. Acta* **74**, 2082–2098 (2010).
31. E. Brisset *et al*., Lateglacial/Holocene environmental changes in the Mediterranean Alps inferred from lacustrine sediments. *Quat. Sci. Rev.* **110**, 49–71 (2015).
32. AERMC, "Etude paléolimnologique sur 8 lacs du district Rhône-Méditerranée. Mise en place d'éléments de référence pour les lacs des 9 Couleurs, d'Anterne, de Chalain, de Lauvitel, Nègre, de Remoray, du Vallon et de Vens 1er, Années 2007-2008" (Tech. Rep. 3112EAFB08, Agence de l'eau Rhône, Méditerranée et Corse, 2008).
33. G. Perrier, La structure des Alpes occidentales déduite des données géophysiques. *Eclogae Geol. Helv.* **7**, 407–424 (1980).
34. S. J. Markich, Uranium speciation and bioavailability in aquatic systems: An overview. *ScientificWorldJournal* **2**, 707–729 (2002).
35. L. M. Och *et al*., Elevated uranium concentrations in Lake Baikal sediments: Burial and early diagenesis. *Chem. Geol.* **441**, 92–105 (2016).
36. F. Elbaz-Poulichet *et al*., A 10,000-year record of trace metal and metalloid (Cu, Hg, Sb, Pb) deposition in a western Alpine lake (Lake Robert, France): Deciphering local and regional mining contamination. *Quat. Sci. Rev.* **228**, 106076 (2020).
37. F. Thevenon, T. Adatte, J. E. Spangenberg, F. S. Anselmetti, Elemental (C/N ratios) and isotopic ($\delta^{15}N_{org}$, $\delta^{13}C_{org}$) compositions of sedimentary organic matter from a high-altitude mountain lake (Meidsee, 2661 m a.s.l., Switzerland): Implications for Late-glacial and Holocene Alpine landscape evolution. *Holocene* **22**, 1135–1142 (2012).
38. F. Chabaux, J. Riotte, O. Dequincey, U-Th-Ra fractionation during weathering and river transport. *Rev. Mineral. Geochem.* **52**, 533–576 (2003).
39. M. B. Andersen, C. H. Stirling, S. Weyer, Uranium isotope fractionation. *Rev. Mineral. Geochem.* **82**, 799–850 (2017).
40. M. B. Andersen, Y. Erel, B. Bourdon, Experimental evidence for ^{234}U–^{238}U fractionation during granite weathering with implications for $^{234}U/^{238}U$ in natural waters. *Geochim. Cosmochim. Acta* **73**, 4124–4141 (2009).
41. L. Missiaen *et al*., Downcore variations of sedimentary detrital $(^{238}U/^{232}Th)$ ratio: Implications on the use of $^{230}Th_{xs}$ and $^{231}Pa_{xs}$ to reconstruct sediment flux and ocean circulation. *Geochem. Geophys. Geosyst.* **19**, 2560–2573 (2018).
42. L. Nuttin, P. Francus, M. Preda, B. Ghaleb, C. Hillaire-Marcel, Authigenic, detrital and diagenetic minerals in the Laguna Potrok Aike sediment sequence. *Quat. Sci. Rev.* **71**, 109–118 (2013).
43. E.-F. Yu, C.-H. Liang, M.-T. Chen, Authigenic uranium in marine sediments of the Benguela current upwelling region during the last glacial period. *Diqiu Kexue Jikan* **10**, 201–214 (1999).
44. J. L. Hinojosa, C. H. Stirling, M. R. Reid, C. M. Moy, G. S. Wilson, Trace metal cycling and $^{238}U/^{235}U$ in New Zealand's fjords: Implications for reconstructing global paleo-redox conditions in organic-rich sediments. *Geochim. Cosmochim. Acta* **179**, 89–109 (2016).
45. M. B. Andersen *et al*., A modern framework for the interpretation of $^{238}U/^{235}U$ in studies of ancient ocean redox. *Earth Planet. Sci. Lett.* **400**, 184–194 (2014).
46. J. M. Rolison, C. H. Stirling, R. Middag, M. J. A. Rijkenberg, Uranium stable isotope fractionation in the Black Sea: Modern calibration of the $^{238}U/^{235}U$ paleo-redox proxy. *Geochim. Cosmochim. Acta* **203**, 69–88 (2017).
47. M. Kalin, W. N. Wheeler, G. Meinrath, The removal of uranium from mining waste water using algal/microbial biomass. *J. Environ. Radioact.* **78**, 151–177 (2005).
48. D. R. Lovley, E. J. P. Phillips, Y. A. Gorby, E. R. Landa, Microbial reduction of uranium. *Nature* **350**, 413–416 (1991).
49. J. D. Wall, L. R. Krumholz, Uranium reduction. *Annu. Rev. Microbiol.* **60**, 149–166 (2006).
50. J. R. Bargar, R. Bernier-Latmani, D. E. Giammar, B. M. Tebo, Biogenic uraninite nanoparticles and their importance for uranium remediation. *Elements* **4**, 407–412 (2008).
51. M. Stylo *et al*., Uranium isotopes fingerprint biotic reduction. *Proc. Natl. Acad. Sci. U.S.A.* **112**, 5619–5624 (2015).
52. S. T. Brown, A. Basu, X. Ding, J. N. Christensen, D. J. DePaolo, Uranium isotope fractionation by abiotic reductive precipitation. *Proc. Natl. Acad. Sci. U.S.A.* **115**, 8688–8693 (2018).
53. S. Szenknect *et al*., First experimental determination of the solubility constant of coffinite. *Geochim. Cosmochim. Acta* **181**, 36–53 (2016).
54. X. Guo *et al*., Thermodynamics of formation of coffinite, $USiO_4$. *Proc. Natl. Acad. Sci. U.S.A.* **112**, 6551–6555 (2015).
55. R. Guillaumont, F. J. Mompean, *Update on the Chemical Thermodynamics of Uranium, Neptunium, Plutonium, Americium and Technetium* (Elsevier Amsterdam, 2003).
56. I. Grenthe *et al*., *Chemical thermodynamics of Uranium* (Elsevier Amsterdam, 1992).
57. H. Veeramani *et al*., Products of abiotic U(VI) reduction by biogenic magnetite and vivianite. *Geochim. Cosmochim. Acta* **75**, 2512–2528 (2011).
58. V. Sivaswamy *et al*., Multiple mechanisms of uranium immobilization by Cellulomonas sp. strain ES6. *Biotechnol. Bioeng.* **108**, 264–276 (2011).
59. D. S. Alessi *et al*., Quantitative separation of monomeric U(IV) from UO_2 in products of U(VI) reduction. *Environ. Sci. Technol.* **46**, 6150–6157 (2012).
60. A. P. Deditius, S. Utsunomiya, R. C. Ewing, The chemical stability of coffinite, $USiO_4 \cdot nH_2O$; $0 < n < 2$, associated with organic matter: A case study from Grants uranium region, New Mexico, USA. *Chem. Geol.* **251**, 33–49 (2008).
61. A. Mesbah *et al*., Coffinite, $USiO_4$, is abundant in nature: So why is it so difficult to synthesize? *Inorg. Chem.* **54**, 6687–6696 (2015).
62. S. Szenknect *et al*., Coffinite formation from UO_{2+x}. *Sci. Rep.* **10**, 12168 (2020).
63. I. Dreissig, S. Weiss, C. Hennig, G. Bernhard, H. Zänker, Formation of uranium(IV)-silica colloids at near-neutral pH. *Geochim. Cosmochim. Acta* **75**, 352–367 (2011).
64. J. Janeczek, R. C. Ewing, Dissolution and alteration of uraninite under reducing conditions. *J. Nucl. Mater.* **190**, 157–173 (1992).
65. S. D. Kelly *et al*., Uranium transformations in static microcosms. *Environ. Sci. Technol.* **44**, 236–242 (2010).
66. S. D. Kelly *et al*., Speciation of uranium in sediments before and after in situ biostimulation. *Environ. Sci. Technol.* **42**, 1558–1564 (2008).
67. S. E. Bone, J. J. Dynes, J. Cliff, J. R. Bargar, Uranium(IV) adsorption by natural organic matter in anoxic sediments. *Proc. Natl. Acad. Sci. U.S.A.* **114**, 711–716 (2017).
68. H. Fu *et al*., Transformation of uranium species in soil during redox oscillations. *Chemosphere* **208**, 846–853 (2018).
69. J. O. Sharp *et al*., Uranium speciation and stability after reductive immobilization in aquifer sediments. *Geochim. Cosmochim. Acta* **75**, 6497–6510 (2011).
70. L. Loreggian, J. Sorwat, J. M. Byrne, A. Kappler, R. Bernier-Latmani, Role of iron sulfide phases in the stability of noncrystalline tetravalent uranium in sediments. *Environ. Sci. Technol.* **54**, 4840–4846 (2020).
71. L. Stetten *et al*., Experimental redox transformations of uranium phosphate minerals and mononuclear species in a contaminated wetland. *J. Hazard. Mater.* **384**, 121362 (2020).
72. S. E. Bone *et al*., Complexation by organic matter controls uranium mobility in anoxic sediments. *Environ. Sci. Technol.* **54**, 1493–1502 (2020).
73. K. V. Lau, T. W. Lyons, K. Maher, Uranium reduction and isotopic fractionation in reducing sediments: Insights from reactive transport modeling. *Geochim. Cosmochim. Acta* **287**, 65–92 (2020).
74. J.-L. Reyss, S. Schmidt, F. Legeleux, P. Bonté, Large, low background well-type detectors for measurements of environmental radioactivity. *Nucl. Instrum. Methods Phys. Res. Sect. Accel. Spectrometers Detect. Assoc. Equip.* **357**, 391–397 (1995).
75. E. D. Goldberg, *Geochronology with ^{210}Pb in Radioactive Dating, Proceedings Series* (International Atomic Energy Agency, 1963), pp. 121–131.
76. M. Blaauw, Methods and code for 'classical' age-modelling of radiocarbon sequences. *Quat. Geochronol.* **5**, 512–518 (2010).

Downloaded from https://www.pnas.org by 81.249.197.186 on March 15, 2023 from IP address 81.249.197.186.

77. R Core Team, *R: A Language and Environment for Statistical Computing, Version 3.6.2* (R Foundation for Statistical Computing, Vienna, Austria, 2019).
78. I. Renberg, R. Bindler, M.-L. Brännvall, Using the historical atmospheric lead-deposition record as a chronological marker in sediment deposits in Europe. *Holocene* **11**, 511–516 (2001).
79. T. O. Richter *et al*., The Avaatech XRF core scanner: Technical description and applications to NE Atlantic sediments. *Geol. Soc. Lond. Spec. Publ.* **267**, 39–50 (2006).
80. E. Douville *et al*., Rapid and accurate U–Th dating of ancient carbonates using inductively coupled plasma-quadrupole mass spectrometry. *Chem. Geol.* **272**, 1–11 (2010).
81. IRMM, *Certificate of Analysis: Isotopic Reference Material IRMM-184* (Institute for Reference Materials and Measurements, Geel, Belgium, 2005).
82. NBL, *Certificate of Analysis: Uranyl Nitrate Assay and Isotopic Solution CRM 145* (New Brunswick Laboratory, U.S. Department of Energy, Argonne, IL, 2010).
83. S. M. Webb, SIXpack: A graphical user interface for XAS analysis using IFEFFIT. *Phys. Scr.* **2005**, 1011 (2005).
84. B. Ravel, M. Newville, ATHENA, ARTEMIS, HEPHAESTUS: Data analysis for X-ray absorption spectroscopy using IFEFFIT. *J. Synchrotron Radiat.* **12**, 537–541 (2005).
85. M. Seder-Colomina *et al*., Uranium(VI) scavenging by amorphous iron phosphate encrusting sphaerotilus natans filaments. *Environ. Sci. Technol.* **49**, 14065–14075 (2015).
86. B. K. Teo, *EXAFS: Basic Principles and Data Analysis* (Springer, Berlin, Heidelberg, 1986).
87. A. L. Ankudinov, B. Ravel, J. J. Rehr, S. D. Conradson, Real-space multiple-scattering calculation and interpretation of X-ray-absorption near-edge structure. *Phys. Rev. B Condens. Matter Mater. Phys.* **58**, 7565–7576 (1998).
88. L. H. Fuchs, E. Gebert, X-ray studies of synthetic coffinite, thorite and uranothorites. *Am. Mineral.* **43**, 243–248 (1958).
89. A. J. Locock, P. C. Burns, Crystal structures and synthesis of the copper-dominant members of the autunite and meta-autunite groups: Torbernite, zeunerite, meta-torbernite and metazeunerite. *Can. Mineral.* **41**, 489–502 (2003).
90. J. Howatson, D. M. Grev, B. Morosin, Crystal and molecular structure of uranyl acetate dihydrate. *J. Inorg. Nucl. Chem.* **37**, 1933–1935 (1975).
91. M. Muñoz, P. Argoul, F. Farges, Continuous Cauchy wavelet transform analyses of EXAFS spectra: A qualitative approach. *Am. Mineral.* **88**, 694–700 (2003).
92. M. Muñoz, F. Farges, P. Argoul, Continuous Cauchy wavelet transform of XAFS spectra. *Phys. Scr.* **2005**, 221 (2005).
93. S. Labs *et al*., Synthesis of coffinite, $USiO_4$, and structural investigations of $U_xTh_{(1-x)}SiO_4$ solid solutions. *Environ. Sci. Technol.* **48**, 854–860 (2014).

Downloaded from https://www.pnas.org by 81.249.197.186 on March 15, 2023 from IP address 81.249.197.186.